

to be presented at Portugal '98 workshop

APPLICATION OF WAVELETS
TO THE ANALYSIS
OF MULTISCALE STRUCTURES

Michael Gedalin
Department of Physics
Ben-Gurion University, Beer-Sheva 84105, Israel

Christopher T. Russell
IGPP/UCLA

ABSTRACT

We demonstrate capabilities of wavelet transform on the measured magnetic field of a collisionless shock. First derivative of Gaussian is applied to the time series to identify the smallest scale of the ramp transition. Morlet transform is used for the local analysis of wave features.

1 Introduction

The standard method of analysis of a time series is Fourier transform, which has a number of drawbacks. For example, it cannot be applied to wavepackets which are only several wavelengths long. Neither can it separate localized structures which contribute into power spectrum independently of their position. Wavelet transform is free of these drawbacks and allows retain information about position and scale (frequency) as well. It is, therefore, an appropriate tool for the analysis of complex systems, which contain a number of different scales and in which stationary localized structures coexist with quasiperiodic time-dependent features. An example of such system is a collisionless shock profile, in which on a presumably sharp gradient of the magnetic field (ramp) large amplitude waves may be superimposed, making identification of the ramp itself and determination of the wave features difficult. In the present paper we apply wavelet transform to a shock profile (magnetic field) to demonstrate capabilities of the method. The emphasis is on the possibility of extracting useful information from a single spacecraft observations without invoking other plasma parameter measurements. We restrict ourselves only to the magnetic vector data. The paper is organized as follows. In section 2 we give theoretical background of the wavelet transform and the method presented in the paper. In section 3 we apply the wavelet transform to the ramp transition region in the shock profiled for the determination of the ramp scale. In section 4 we apply Morlet transform for the local determination of the

upstream and downstream wave properties in the same shock profile.

2 Theoretical Background

Any localized function $\psi(t)$, so that $\int_{-\infty}^{\infty} |\psi|^2 dt < \infty$, can be chosen as a mother wavelet, if it satisfies the admissibility criterion $\int_{-\infty}^{\infty} \psi dt = 0$. If this is a case, a family of the wavelets is built according to the following prescription:

$$\psi[a, d](t) = d^{-1/2} \psi\left(\frac{t-a}{d}\right), \quad (1)$$

where a is the position of the wavelet and d is its scale.

For any $f(t)$ its wavelet transform $W[f](a, d)$ is defined as follows:

$$W[f](a, d) = \int_{-\infty}^{\infty} f(t) \psi^*[a, d](t) dt. \quad (2)$$

In reality $f(t)$ is not a continuous function but a time series, so that integration in (2) should be substituted by summation. An obvious immediate advantage of the method is that the time series does not have to be stationary, and there is no need to detrend it.

It is clear that the result of the transform depends on the choice of the mother wavelet (in general, arbitrary except the admissibility condition), so that this choice should be dictated by our goals. In what follows we will be interested in the analysis of two different features, which in the ideal case look as a) a sharp jump of the magnetic field, or b) monochromatic wave. It has been shown that the first derivative of Gaussian (G1)

$$G_1(t) = t \exp(-t^2/2) = (-d/dt) \exp(-t^2/2) \quad (3)$$

is especially suitable for the identification of the features of the first kind, while waves are best analyzed with the use of the complex Morlet (M) wavelet:

$$M(t) = \exp(2\pi it - t^2/2). \quad (4)$$

Let us consider the two wavelet transforms in more detail. In the lowest order approximation a sharp jump can be represented as a step function $f(t) = H(t - t_0)$, where $H(t) = 1$ when $t > 0$ and $H(t) = 0$ otherwise. The corresponding G1-transform looks as follows:

$$W_G[H](a, d) = d^{1/2} \exp\left[-\frac{(t_0 - a)^2}{2d^2}\right]. \quad (5)$$

In what follows we shall use the wavelet power spectrum $P = |W|^2/d$, which in this case takes the following form:

$$P_G[H](a, d) = \exp\left[-\frac{(t_0 - a)^2}{d^2}\right], \quad (6)$$

and has a sharp maximum at $a = t_0$, independently of d , while the isocontours (lines of $P = \text{const}$ on the $a - d$ plane) are $|a - t_0|/d = \text{const}$.

In reality the transition is never infinitely narrow. Let us approximate the transition by $f(t)$ such that $df/dt = (2\pi)^{-1/2}D^{-1} \exp[-(t - t_0)^2/2D^2]$. When $D \rightarrow 0$ our $f(t) \rightarrow H(t - t_0)$. The corresponding power spectrum is

$$P_G[f](a, d) = \frac{d^2}{d^2 + D^2} \exp\left[-\frac{(t_0 - a)^2}{d^2 + D^2}\right]. \quad (7)$$

Isocontours are $|a - t_0|/d \approx \text{const}$ when $d \gg D$, and $|a - t_0| \propto \ln d$ when $d \ll D$. Thus, the scale, where the conic isocontours $|a - t_0|/d \approx \text{const}$ break down, gives the width D of the profile.

Let us now examine a monochromatic wave $f(t) = \cos(\omega t)$. The G-transform gives

$$P_G(a, d) = \omega^2 d^2 \sin^2(\omega a) \exp(-\omega^2 d^2/2), \quad (8)$$

which is small for small and large values of d as well. We conclude that the G-transform is not sensitive to monochromatic waves.

Let us consider now the M-transform of a monochromatic wave $f = \cos(\omega t)$. The transform is easily calculated:

$$W_M(a, d) = \sqrt{\frac{\pi d}{2}} [\exp(i\omega a - (\omega d - 2\pi)^2/2) + \exp(-i\omega a - (\omega d + 2\pi)^2/2)]. \quad (9)$$

The second term in square brackets is always small and we shall neglect it hereforth. Then the spectral power is

$$P_M(a, f) = \frac{\pi}{2} \exp[-4\pi^2(f_0/f - 1)^2], \quad (10)$$

where we defined $f_0 = \omega/2\pi$ and $f = 1/d$. It is easy to see that the spectral power has a sharp maximum at $f = f_0$.

In reality wavepackets are always of a finite length, so we examine the M-transform of the following wavepacket: $f = \exp[i\omega(t - t_0) - (t - t_0)^2/2T^2]$. The spectral power is easily calculated in the following form:

$$P_M(a, f) = \frac{d^2 + T^2}{\exp} [-2\pi^2 K^2 (f_0 - f)^2 - (a - t_0)^2/2(d^2 + T^2)], \quad (11)$$

where, as above, $f_0 = \omega/2\pi$, $f = 1/d$, and $K^{-2} = d^{-2} + T^{-2}$. Again there is a sharp maximum at $f = f_0$ for fixed a . We can also estimate the temporal width Δ_a of the M-transform (which is centered on $a = t_0$ as is the initial wavepacket) and uncertainty in the frequency determination Δ_f/f_0 as follows:

$$\Delta_a = \sqrt{d^2 + T^2} \approx \sqrt{1 + (f_0 T)^2}/f_0, \quad (12)$$

$$\Delta_f/f_0 = \frac{1}{2\pi K} \approx \frac{1}{2\pi} \sqrt{1 + (f_0 T)^{-2}}, \quad (13)$$

which shows that when $f_0 T \gg 1$ the temporal width of the M-transform equals the width of the wavepacket, and the uncertainty of the frequency determination is $1/2\pi$. Expressions (12)–(13) show that even when $f_0 T \sim 1$, that is, when the wavepacket is short and contains only ~ 1 waveperiod, the precision of the determination of its parameters using the M-transform is rather good.

As is seen from this analysis, the M-transform of a wavepacket looks as a stripe in the $a - -f$ plane, which is parallel to a -axis. It can be shown that the M-transform of the step-like profiles looks as a "fan" diverging to large d and can be easily separated from the wave features.

In what follows we plan to apply M-transform to the measurements of the magnetic field vector $\mathbf{B} = (B_x, B_y, B_z)$. As can be seen from above, the M-transform effectively extracts quasi-monochromatic wave packets, and $W_i \equiv W_M[B_i](a, f) = B_i q(a, d)$, where $i = x, y, z$ and function $f(a, d)$ is the same for all three components. Thus, we can treat $\mathbf{W} = (W_x, W_y, W_z)$ locally as a magnetic field of a monochromatic wave (apart of insignificant common factor q).

Let us consider such a wave, in which $\mathbf{B} = \mathbf{B}_1 + i\mathbf{B}_2$, where B_1 and B_2 are real. Presence of i means phase shift of $\pi/2$. It can be shown that the usual definition of the degree of circular polarization P_c can be reformulated in the vector form as follows:

$$P_c = \frac{2|\mathbf{B}_1 \times \mathbf{B}_2|}{\mathbf{B} \cdot \mathbf{B}^*}, \quad (14)$$

and, if $P_c \neq 0$, the propagation direction is given by the following unity vector:

$$\hat{\mathbf{n}} = \frac{\mathbf{B}_1 \times \mathbf{B}_2}{|\mathbf{B}_1 \times \mathbf{B}_2|}. \quad (15)$$

Translating this into the language of M-transform, one finds

$$P_c = \frac{2|\text{Im } \mathbf{W} \times \text{Re } \mathbf{W}|}{\mathbf{W} \cdot \mathbf{W}^*}, \quad (16)$$

$$\hat{\mathbf{n}} = \frac{\text{Im } \mathbf{W} \times \text{Re } \mathbf{W}}{|\text{Im } \mathbf{W} \times \text{Re } \mathbf{W}|}. \quad (17)$$

It is worth noting that because of the nature of the wavelet transform \mathbf{W} is always completely polarized and the degree of linear polarization $P_l = 1 - P_c$.

3 Ramp Identification

In this section we apply the G-transform to the magnetic field profile of the s0292 shock. The total magnetic field and components are shown in Figure 1. Figure 2 shows the wavelet spectral power for G1 and M-transforms applied to the central part of the magnetic field profile. The G-transform panel clearly shows the ramp transition and two more distinct step-like features downstream. The

M-transform panel shows presence of downstream turbulence in two frequency ranges (see below). Figure 3 shows the G-transform in more detail. The ramp transition is identified from the typical conic shape of the transform. The ramp is at $t = 620$ s and its width is about 2 s.

4 Upstream and Downstream Waves

In this section we study upstream and downstream waves using the method described in section 2. The corresponding regions under consideration are shown in Figure 1 by vertical lines.

For each component of the magnetic field B_i we find the corresponding M-transform $W_i(a, f)$, where $f = 1/d$, and the spectral power matrix is defined as $P_{ij}(a, f) = fW_i \cdot W_j^*$. The total power is defined as $P_t = P_{xx} + P_{yy} + P_{zz}$. The total spectral power and spectral power for each component for upstream waves are shown in Figure 4. It is seen that the distribution of the wave power is inhomogeneous. The strongest wave activity lasts for only several periods. It is also seen that the wave activity in B_y is weak, while other components behave differently in different places. Figure 5 shows the wavelet analog of cross-correlation spectral power. In both figures the range with $P_t < 0.2 \max(P_t)$ are cut out to make the presentation more clear.

Figure 6 presents the polarization parameters of the upstream waves. In the upper panel we provide the total magnetic field which has been denoised using the Daubechies-10 wavelet transform and removing 7 finest levels. This magnetic field is used below as a background magnetic field for the calculation of the angle of the propagation direction with the magnetic field (the lowest panel). The other panels show the total spectral power (for reference) and the degree of circular polarization. It should be noted that the determination of the angle $\phi = \arccos |\hat{\mathbf{n}} \cdot \mathbf{b}|$ (where $\mathbf{b} = \mathbf{B}/|\mathbf{B}|$) is reliable only when the circular polarization is substantial. It is clearly seen that in the regions, where circular polarization is high, the waves propagate at small angles with respect to the background magnetic field. In Figure 7 the direction of propagation is given via angles between $\hat{\mathbf{n}}$ and axes x , y , and z . The direction of propagation is rather stable, that is, does not fluctuate rapidly. This stability is necessary for reliability of the method.

In principle, knowing direction of the wavevector \mathbf{k} (which coincides with $\hat{\mathbf{n}}$) and the plasma velocity in the spacecraft frame \mathbf{V} , one may estimate the plasma rest frame frequency of these waves from the Doppler shift $\omega' = |\omega - \mathbf{k} \cdot \mathbf{V}|$, invoking theoretically known dispersion relations. We will not discuss this subject in more details here.

Figures 8–12 show the results of similar analysis for downstream waves. We shall briefly comment the main peculiarities. In this region there are two distinct frequency ranges of wave activity. Higher frequency is close to the spacecraft rotation frequency $1/3 \text{ s}^{-1}$ (shown in Figures 8–10 by green line) and to the ion gy-

rofrequency as well (shown in Figure 10 by red line). The first proximity makes one suspect that this is an artifact (although that may be a mere coincidence), therefore we choose to not analyze it here and restrict ourselves to the lower frequency band in Figures 11 and 12. In this frequency range the waves are strongly circularly polarized ($P_c > 0.7$ typically) and propagate preferentially along the background magnetic field. The angles between \mathbf{k} and axes are also very stable and vary relatively weakly, although this variation is quite noticeable.

5 Conclusions

We demonstrated capabilities of local analysis of a complex multiscale system using wavelets. We have shown that G1 wavelet can be used to identify positions and determine widths of steplike features. We have also proposed a method of local determination of wave polarization and direction of its propagation. The clear advantage of the method is that it does not require spatial (temporal) averaging, necessary for Fourier analysis, thus allowing retain high temporal resolution along with a rather good frequency resolution, even for short wavepackets containing only few waveperiods.

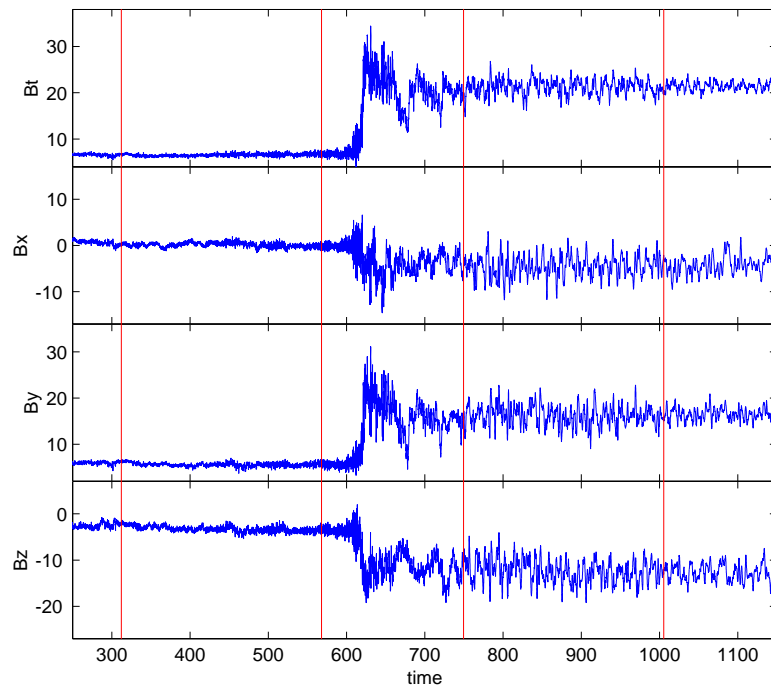


Figure 1: Total magnetic field and components for the shock s0292. Time in seconds starting from an arbitrary moment. Vertical lines cut out the upstream and downstream regions studied later in section 4.

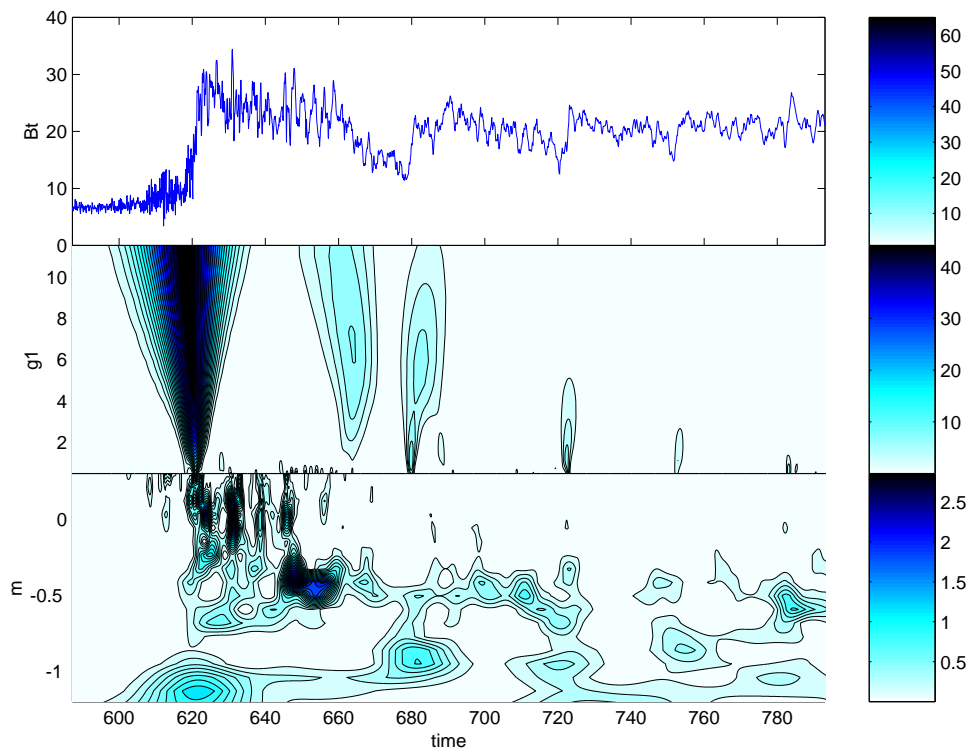


Figure 2: Total magnetic field and contour plots for G1 and M-transforms for the central part of the s0292 shock.

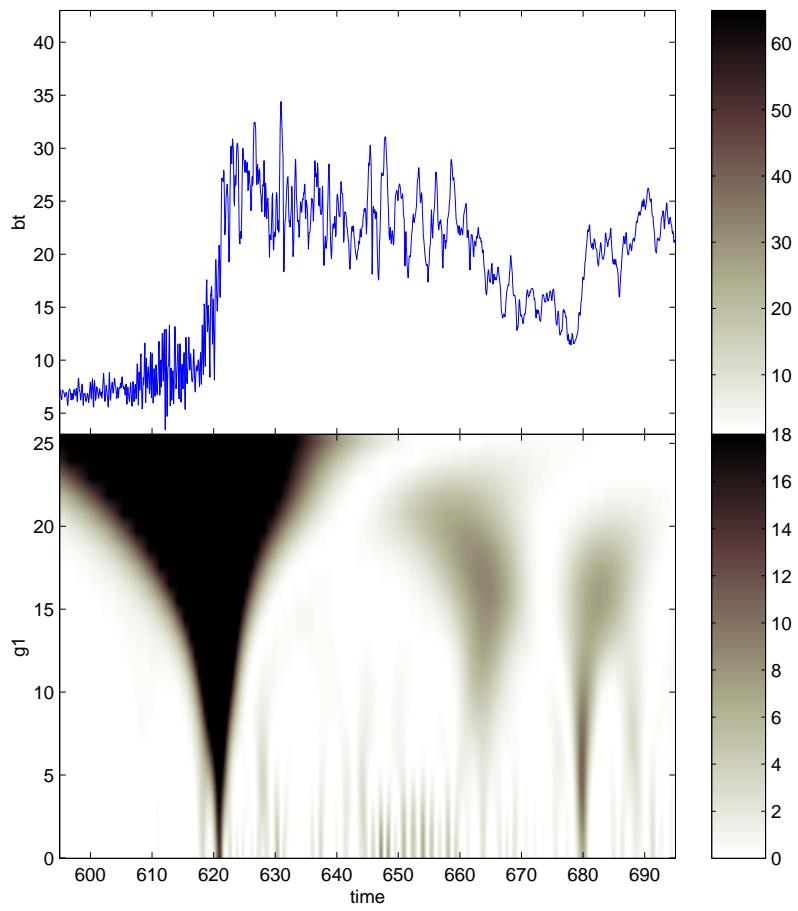


Figure 3: Total magnetic field and contour plot for G1-transform for the central part of the s0292 shock – more detailed view.

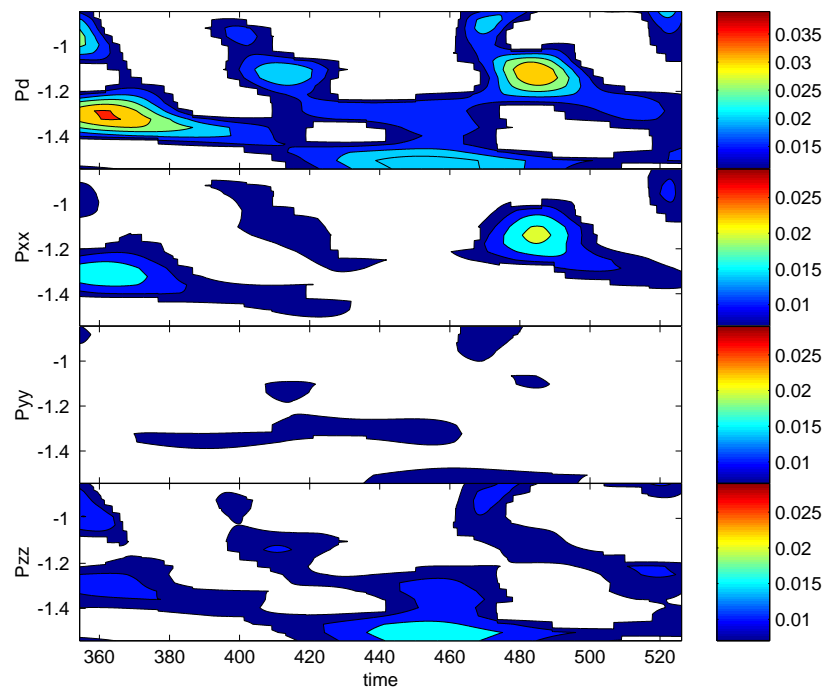


Figure 4: Spectral power $P_{ii} = W_i \cdot W_i^*/d$ for upstream waves.

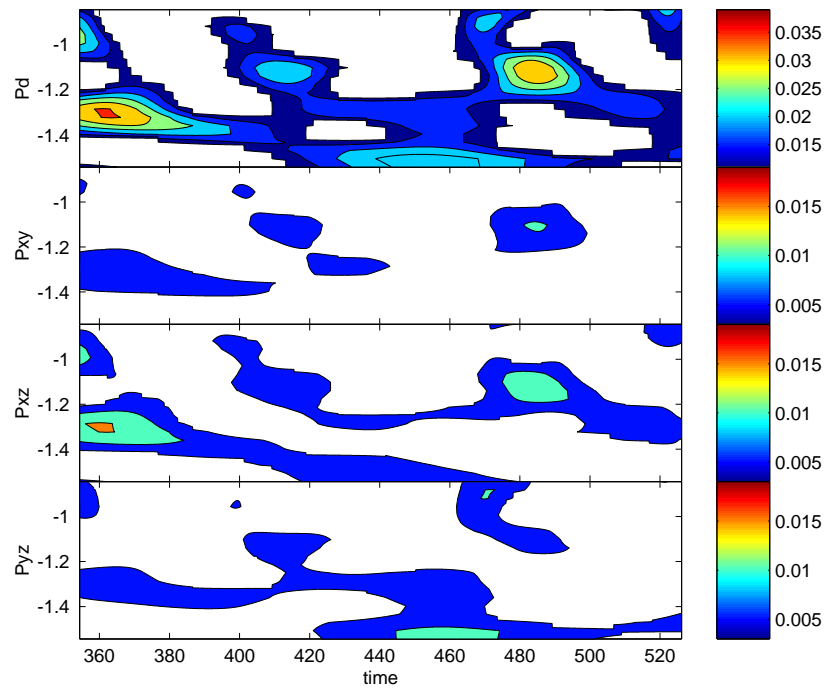


Figure 5: Cross-correlation spectral power $|P_{ij}| = |W_i \cdot W_j^*|/d, i \neq j$ for upstream waves.

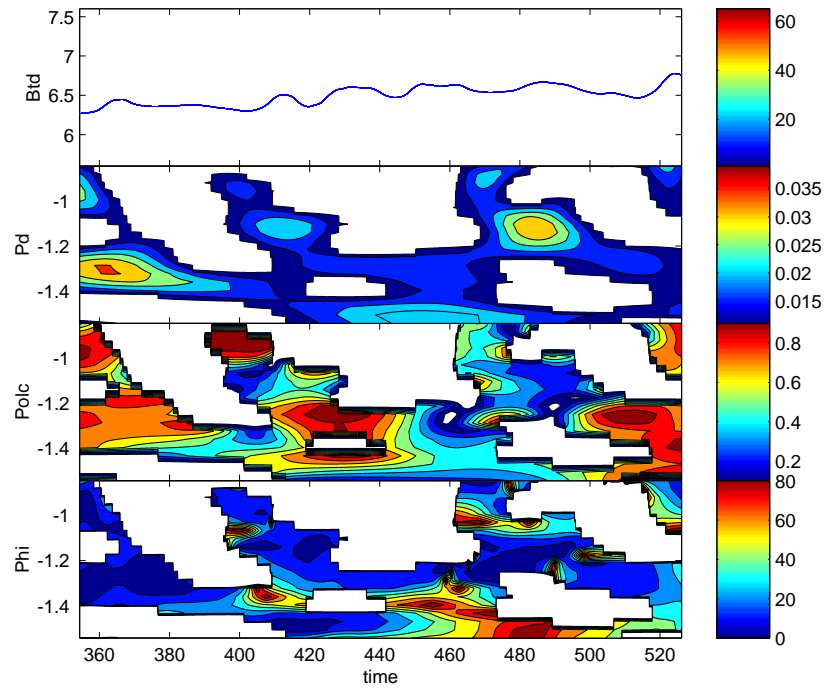


Figure 6: From top to bottom: a) total magnetic field with fluctuations filtered out using Daubechies-10 wavelet transform and removing 7 finest scales, b) total wavelet spectral power, c) degree of circular polarization, and d) angle between the direction of propagation and the denoised magnetic field.

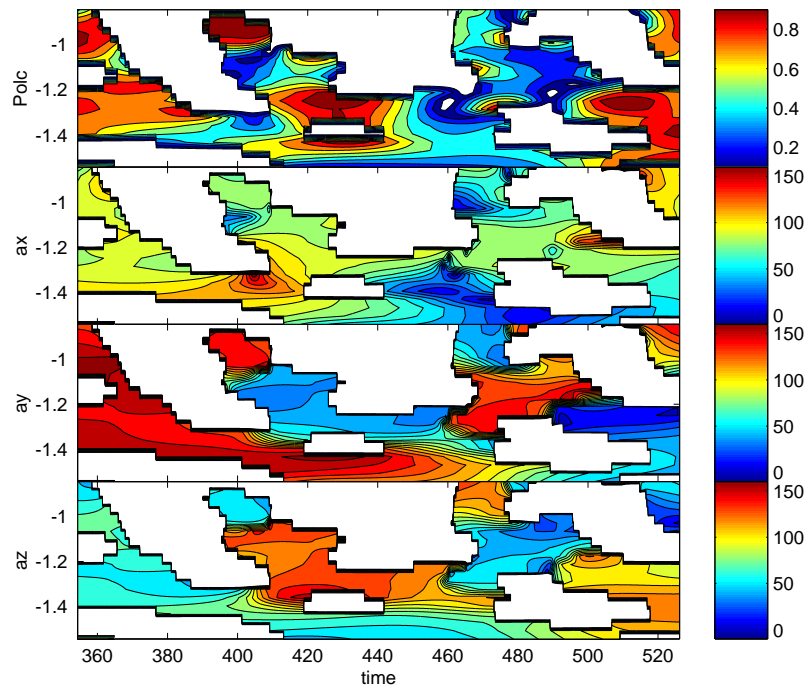


Figure 7: Degree of circular polarization (upper panel) and angles between the direction of propagation \hat{n} and axes x , y , and z .

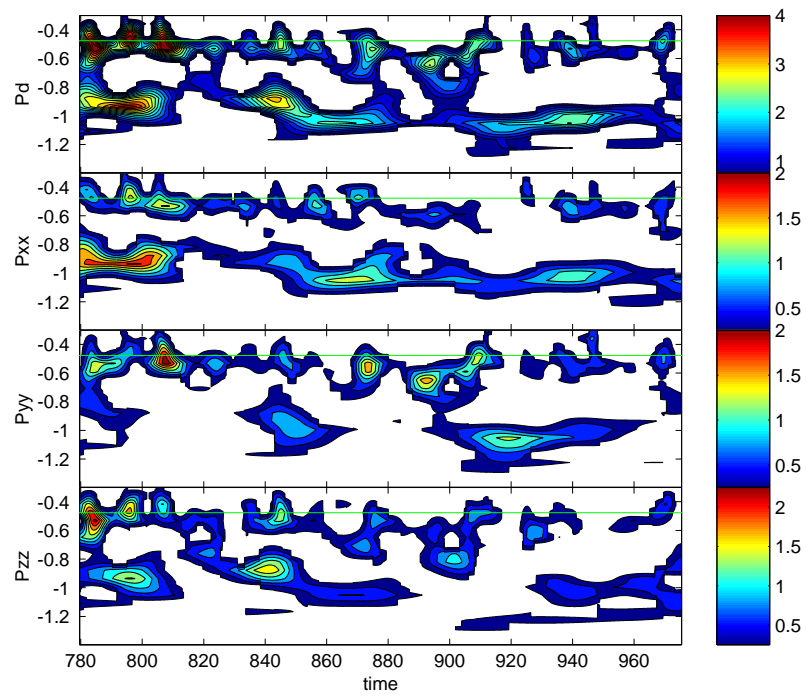


Figure 8: Spectral power $P_{ii} = W_i \cdot W_i^*/d$ for downstream waves.

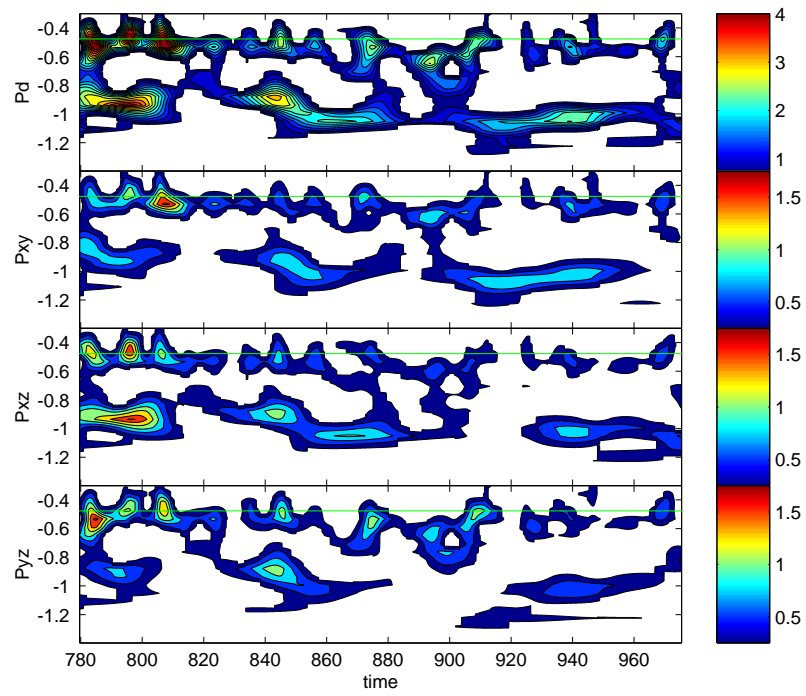


Figure 9: Cross-correlation spectral power $|P_{ij}| = |W_i \cdot W_j^*|/d, i \neq j$ for downstream waves.

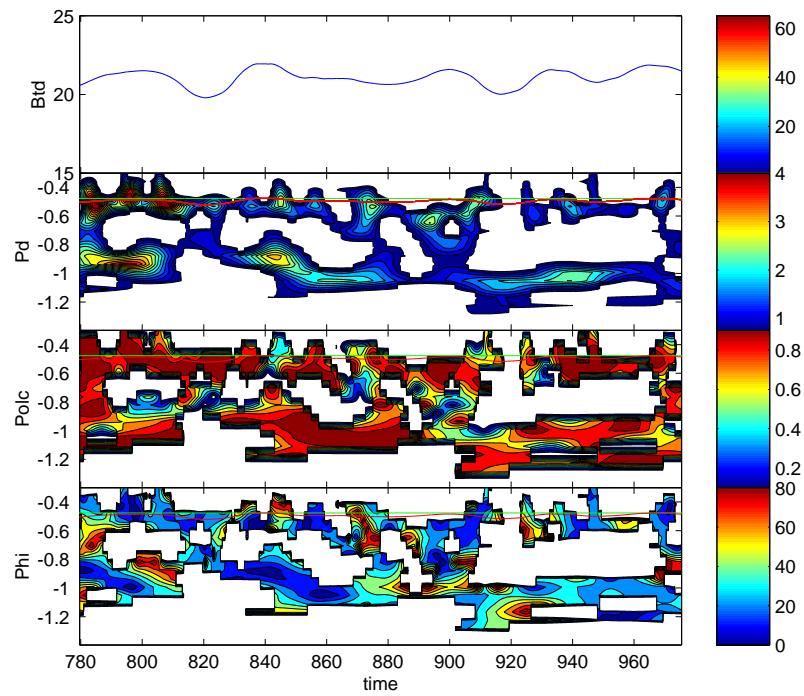


Figure 10: From top to bottom: a) total magnetic field with fluctuations filtered out using Daubechies-10 wavelet transform and removing 7 finest scales, b) total wavelet spectral power, c) degree of circular polarization, and d) angle between the direction of propagation and the denoised magnetic field.

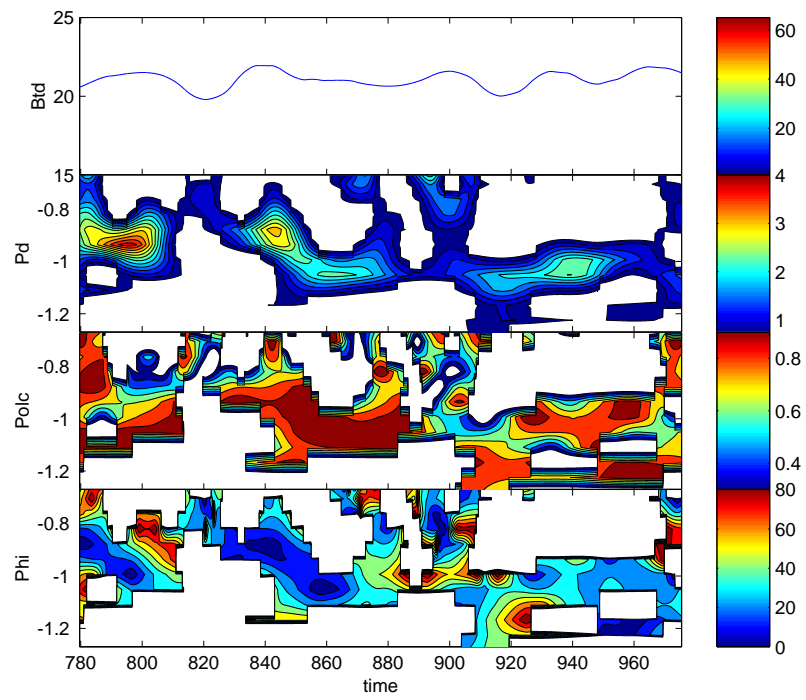


Figure 11: Same as in Figure 10 but for low frequencies only.

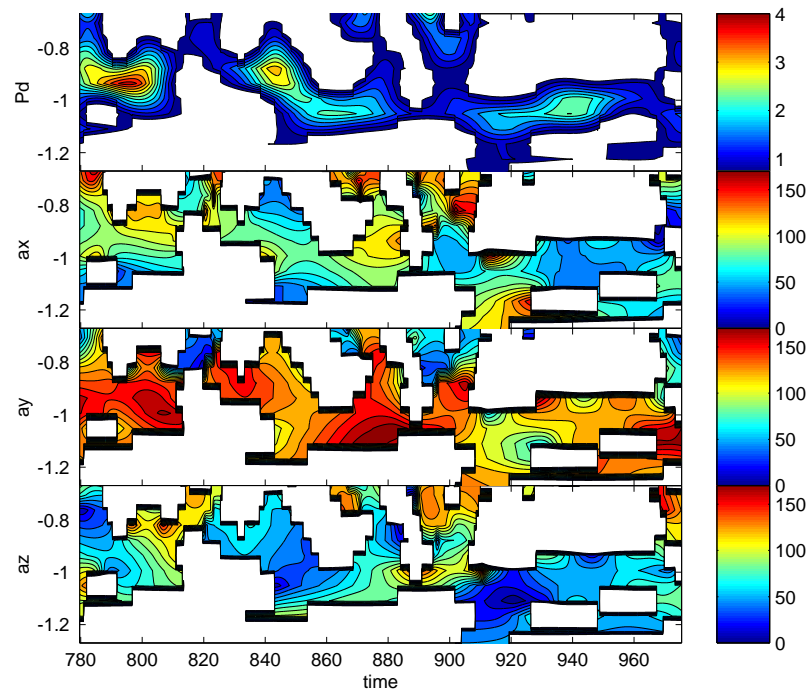


Figure 12: Degree of circular polarization (upper panel) and angles between the direction of propagation \hat{n} and axes x , y , and z .